Chemical Science

ROYAL SOCIETY OF CHEMISTRY

EDGE ARTICLE

View Article Online
View Journal | View Issue

Cite this: *Chem. Sci.*, 2024, **15**, 14195

All publication charges for this article have been paid for by the Royal Society of Chemistry

Initiating a composite membrane with a localized high iodine concentration layer based on adduct chemistry to enable highly reversible zinc–iodine flow batteries†

Yichan Hu,‡[abc] Tao Hu,‡[a] Yuanwei Zhang,[d] Haichao Huang,[d] Yixian Pei,[d] Yihan Yang,[e] Yudong Wu,[a] Haibo Hu,*[a] Guojin Liang*[bd] and Hui-Ming Cheng[bd]

The issue of polyiodide crossover at an iodine cathode significantly diminishes the efficiency and practicality of aqueous zinc–iodine flow batteries (ZIFBs). To address this challenge, we have introduced a localized high iodine concentration (LHIC) coating layer onto a porous polyolefin membrane, which featured strong chemical adsorption by exploiting adduct chemistry between the iodine species and a series of low-cost oxides, *e.g.*, MgO, CeO_2, ZrO_2, TiO_2, and Al_2O_3. Leveraging the LHIC based on the potent iodine adsorption capability, the as-fabricated MgO-LHIC composite membrane effectively mitigates iodine crossover *via* Donnan repulsion and concentration gradient effects. At a high volumetric capacity of 17.8 Ah L^{-1}, ZIFBs utilizing a MgO–LHIC composite membrane exhibited improved coulombic efficiency (CE) and energy efficiency (EE) of 96.3% and 68.6%, respectively, along with long-term cycling stability of 170 cycles. These results significantly outperform those of ZIFBs based on a blank polyolefin membrane (78.2%/61.9% after 60 cycles) and the widely used commercial Nafion N117 (67.8%/53.0% after 23 cycles). Even under high-temperature conditions (60 °C), the LHIC-based battery still demonstrates superior CE/EE of 95.1%/67.5% compared to those of the blank polyolefin membrane (CE/EE: 61.1%/46.8%). Our pioneering research showcases enormous prospects for developing high-efficiency and low-cost composite membranes based on adduct chemistry for large-scale energy storage applications.

Received 25th June 2024
Accepted 5th August 2024

DOI: 10.1039/d4sc04206a

rsc.li/chemical-science

Introduction

Large-scale and low-cost energy storage is a crucial technology in addressing the intermittent and unstable nature of renewable energy sources like wind and solar energy, thereby enhancing their utilization efficiency.[1–5] Flow batteries (FBs) have emerged as promising candidates with design flexibility, excellent scalability, and decoupled power and energy characteristics.[6–10] Among them, zinc–iodine flow batteries (ZIFBs) have garnered significant attention due to their low cost, intrinsic safety, and superior electrochemical performance.[11–15] However, the issue of polyiodide I_x^- cross-over in ZIFBs, particularly at a high areal capacity, results in continuous capacity loss, leading to low coulombic efficiency (CE) and low energy efficiency (EE) (Fig. 1a and b).[16–19] In addition, FBs as large-scale energy storage systems would be integrated with outdoor clean energy conversion systems which inevitably expose them to high-temperature environments, where the high temperature would exacerbate the shuttling of active polyiodide anions across the membrane resulting in inferior CE and EE of the ZIFBs.[20–22]

Enhancing the selectivity of the membrane can effectively avoid shuttling in ZIFBs at both normal and high temperatures. While relatively expensive fluorinated Nafion membranes are widely used in flow battery systems due to their good selectivity to enable high CE, they feature limited permeability for the cations in ZIFBS, leading to inferior voltage efficiency (VE) at high current densities and compromising the EE and power density in ZIFBs.[23–27] On the other hand, low-cost porous polyolefin membranes have emerged as a viable alternative membrane candidate for improved power, offering good permeability but featuring inferior selectivity.[28–31] To improve

[a]*School of Materials Science and Engineering, Anhui University, Hefei 230601, China. E-mail: haibohu@ahu.edu.cn*

[b]*Faculty of Materials Science and Energy Engineering, Shenzhen University of Advanced Technology, Shenzhen 518055, China. E-mail: gj.liang@siat.ac.cn*

[c]*School of Materials Science and Engineering, Hunan University, Changsha 410000, China*

[d]*Institute of Technology for Carbon Neutrality, Shenzhen Institute of Advanced Technology, Chinese Academy of Sciences (CAS), Shenzhen 518055, China*

[e]*School of Physics and Electronics, Hunan University, Changsha 410000, China*

† Electronic supplementary information (ESI) available. See DOI: https://doi.org/10.1039/d4sc04206a

‡ These authors contributed equally.

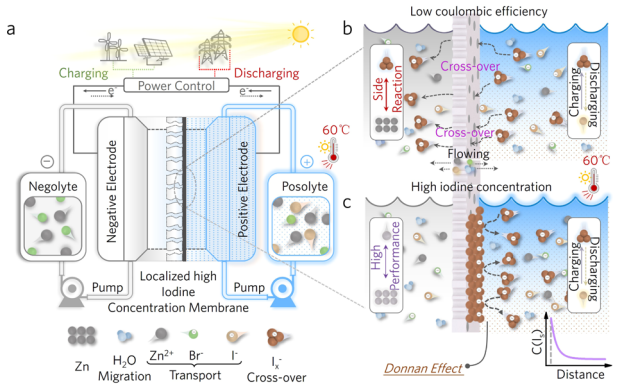

Fig. 1 Different processes in ZIFBs with a porous polyolefin membrane and a LHIC composite membrane. (a) Schematic of a ZIFB employing $ZnBr_2$ as the negolyte and ZnI_2 as the posolyte. (b) Cross-over of I_x^- through the porous polyolefin membrane would lead to rapid cell failure of ZIFBs. (c) A LHIC composite membrane repels the negatively charged active materials (I_x^-) from cross-over owing to the negatively charged MgO layer.

the selectivity of porous polyolefin membranes, one applicable strategy in different FB systems is constructing a composite membrane by introducing a selectively sieving coating layer onto the membranes, where the working principle is generally based on the size-sieving effect and the Donnan effect. Specifically, the size-sieving materials utilized are finely tailored in structure and size, such as zeolites,[32] metal–organic frameworks,[33] polyamides,[34] and two-dimensional materials.[35,36] These coating materials would be correlated to complex synthesis steps with high costs to construct a precise and selective ion transport pathway. On the other hand, regarding the Donnan effect, Lu *et al.* recently developed a one-step low-cost but highly effective strategy to introduce the common Ketjen black (KB) as an adsorption layer to concentrate the polysulfide anions on the membrane surface,[37] where a localized high concentration layer of the active species was constructed with strong electrostatic repulsion based on the Donnan effect. Consequently, the cross-over issue of polysulfide/polyiodide was effectively suppressed to obtain improved CE and enhanced cycling stability of the iodine–sulfur FBs. Inspired by this concept, the introduction of a localized high iodine concentration (LHIC) layer onto the membrane of ZIFBs could accommodate the concentration gradient effect and the Donnan effect, which was highly possible to solve the cross-over issue of polyiodide anions. However, despite the effectiveness of applying LHIC to prevent the shuttling of active species, there have been few attempts to develop a LHIC coating layer in ZIFB systems to inhibit the cross-over issue of charged iodine species.

Previously, Klabunde and colleagues[38,39] reported a series of low-cost and sustainable oxides that exhibit strong physicochemical adsorption towards halogens, forming halogen–oxide adducts with strong halogen adsorption capability as effective halogen carriers in antimicrobial applications. Taking advantage of the strong adsorption properties between the oxides and iodine, it has high potential to construct a LHIC coating layer onto a porous polyolefin membrane, where the selectivity of the porous polyolefin membrane for active iodine species in ZIFBs could be enhanced as illustrated in Fig. 1c.

Here, a series of effective LHIC coating layers based on iodine–oxide adducts were developed and introduced onto a porous membrane. The research on the stability of a series of oxide–halogen adducts, such as MgO, CeO_2, ZrO_2, TiO_2, and Al_2O_3, revealed that MgO–iodine adducts exhibited the highest iodine adsorption energy to enable the most effective LHIC layer. Consequently, the LHIC composite membrane based on MgO nanoparticles featured superior Donnan exclusion and concentration gradient effects to limit polyiodide (I_x^-) shuttling and mitigate the capacity loss problem of ZIFBs, achieving improved CE and long-term cycle stability. This study presents a cost-effective and feasible implementable strategy for tackling the longstanding challenge of polyiodide capacity loss, thereby enhancing the practical viability of ZIFBs for large-scale and low-cost energy storage.

Results and discussion

Adsorption stability of different oxide–iodine adducts

The iodine–oxide adducts were prepared by one-step mixing of commercial oxides with the iodine catholyte solution at a simulated 50% state of charge, where the active iodine species, *i.e.*, polyiodides as I_3^- and I_5^-, could undergo strong chemical adsorption with the oxides. Ideally, the stronger the adsorption ability, the more stable the oxide–iodine adducts, which is also more conducive to constructing long-term stable LHIC coating. Specifically, according to the digital image of the as-obtained adducts, MgO exhibited the deepest color such as dark brown (Fig. 2a). In contrast, slight color differences are observed among the other oxides, indicating that MgO had the strongest adsorption capability (Fig. 2a). To investigate the adsorption capacity of different oxides, the oxide–polyiodide mixture was placed in a 70 °C oven to evaporate the I_2 species to obtain the mass retention plot shown in Fig. 2b. It is worth noting that after drying for 72 hours, the iodine mass retention ratio based on MgO was up to 90.81%, which was significantly higher than those of other oxides (56.1% for Al_2O_3, 60.8% for TiO_2, 61.0% for ZrO_2, and 71.7% for CeO_2). With the prolongation of drying time, only the color of MgO remained unchanged as shown in Fig. S1,† while the colors of other oxide-based adducts faded to varying degrees. This indicates that MgO has a strong and long-lasting adsorption capacity for iodine. The XRD peak at 18.5° assigned to iodine is maintained throughout the evaporation process for 72 h (Fig. 2c and S2†), which did not appear in the remaining oxides. Moreover, no apparent changes were observed in the morphology of different oxides after different drying times (Fig. S3–S7†). Taken together, these results indicate that MgO has the strongest adsorption interactions with iodine to form stable adducts.

Furthermore, the adducts were analyzed by Raman spectroscopy, and the normalized data showed a gradual decrease in the I_5^-/I_3^- ratio with increasing drying time. This ratio decrease can be attributed to the reduction in adsorption capacities of different oxides for polyiodides, where weaker adsorption

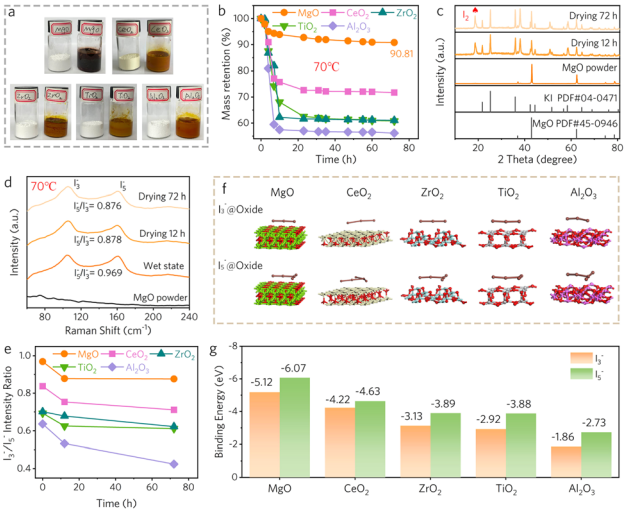

Fig. 2 (a) Optical photographs of different pristine oxides and the adsorbed adducts. (b) Iodine mass retention in different adducts by placing at 70 °C for different durations. (c) XRD profiles of MgO and the MgO–iodine adduct with the drying duration. (d) Raman spectra of the MgO–iodine adduct with different drying durations. (e) The ratio variations of I_3^-/I_5^- in different oxide–iodine adducts with different drying durations according to the Raman results in Fig. S8.† (f) Adsorption configurations of polyiodides on different oxides, respectively. (g) Comparison of adsorption energies with I_3^- and I_5^- in different adducts, respectively.

corresponded to iodine volatilization. After 72 hours of drying, the Raman peak intensity ratio of the I_5^-/I_3^- based on MgO (0.876) was significantly higher than those of Al_2O_3 (0.424), TiO_2 (0.611), ZrO_2 (0.622), and CeO_2 (0.711) (Fig. 2d, e and S8†). To explain the intrinsic reason for the strong adsorption capability of MgO, molecular dynamics simulations were employed to calculate the binding energies between oxides and polyiodide anions (such as I_3^- and I_5^-), and the corresponding stable adsorption configurations are illustrated in Fig. 2f. The results revealed that MgO exhibited the largest molecular adsorption energy with binding energies of −5.12 eV and −6.07 eV for I_3^- and I_5^-, respectively (Fig. 2g). In contrast, the binding energies of CeO_2 (−4.22 eV, −4.63 eV), ZrO_2 (−3.13 eV, −3.89 eV), TiO_2 (−2.92 eV, −3.88 eV), and Al_2O_3 (−1.86 eV, −2.73 eV) are lower than those of MgO. These results align with the previous experimental observations that the MgO–iodine adducts are the most stable ones.[38,39] Therefore, MgO–iodine adducts could have high potential to construct long-term stable composite membranes with high iodine concentration.

Permeability and ion selectivity of LHIC composite membranes

Subsequently, the iodine–oxide adducts were coated onto a porous polyolefin membrane to construct the LHIC-composite membranes (details are provided in the Experimental section), and their corresponding permeability and ion selectivity were investigated. Specifically, different metal oxide-based LHIC composite membranes were prepared using an identical protocol and marked as X-LHIC composite membranes, where X represents different oxides, and a blank porous polyolefin membrane was comparatively studied. The composite membranes with different loading contents of MgO were evaluated using the rate performance of ZIFBs, where the one with the content loading of 2 mg cm^{-2} exhibited superior CE and EE performance (Fig. S9†). Consequently, the 2 mg cm^{-2}-loaded membranes were thereafter applied to evaluate the battery performance for different X-LHIC composite membranes. First, permeation experiments followed the protocol illustrated in Fig. S10†, wherein the inhibition of iodine species cross-over issue by different LHIC-composite membranes can be observed, and UV-vis spectra of the permeation side after different durations are shown in Fig. S11.† More specifically, the MgO-LHIC-based composite membrane demonstrated highly effective suppression of iodine permeation after 48 hours, and the permeation side color remained almost transparent (Fig. 3a), with a much lower absorbance (0.031) than those of other X-LHIC composite membranes (Fig. S12–S16†). Based on these permeation results, the plots of $-\ln(1-C_B/C_A)$ *vs.* permeation time for different X-LHIC composite membranes are shown in Fig. 3b, where calculations were performed to quantify the permeability of these membranes, as presented in Fig. 3c. The permeability of MgO-LHIC is as low as 8.9×10^{-8} cm^2 min^{-1}, which was significantly lower than those of $CeO_2/ZrO_2/TiO_2/Al_2O_3$-LHIC ($9.8 \times 10^{-7}$, 4.5×10^{-6}, 4.5×10^{-6}, and 9.6×10^{-7} cm^2 min^{-1}, respectively) and the blank porous polyolefin membrane (3.4×10^{-5} cm^2 min^{-1}). Thus, these results demonstrate that the

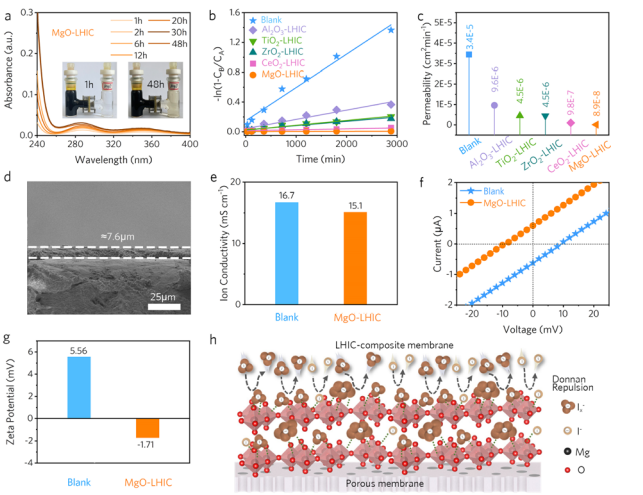

Fig. 3 (a) UV-vis analysis of the permeate side based on the MgO-LHIC composite membrane. The inset shows the corresponding optical photographs. (b) The I_x^- permeability through different membranes in blank 1 M KI_x. The fits of the $-\ln(1-C_B/C_A)$ *vs.* *t* (time) plots were obtained by linear fitting. (c) The corresponding permeability of different X-LHIC composite membranes. (d) SEM cross-section of the MgO-LHIC composite membrane. (e) Comparison of ionic conductivities between the porous polyolefin membrane and MgO-LHIC composite membrane. (f) *I*–*V* curves of the blank porous polyolefin membrane and MgO-LHIC membrane. (g) Zeta potential of the porous polyolefin membrane and the MgO-LHIC composite membrane. (h) Donnan repulsion diagram of the MgO-LHIC composite membrane.

MgO-LHIC composite membrane exhibits the best anti-iodine permeability to deliver the improved electrochemical performance of the ZIFBs.

The cross-sectional SEM image of the prepared MgO-LHIC composite membrane is shown in Fig. 3d, where the thickness of the MgO-LHIC coating layer was 7.6 μm. Even though the introduction of hydrophobic poly(vinylidene fluoride) as a binder could unavoidably increase the contact angle of MgO-LHIC composite membranes, through proper control of the mass ratio, the contact angles of MgO-LHIC (72.1°) and porous polyolefin membranes (69.4°) were comparable that the ion transport would not be largely influenced (Fig. S17†). Moreover, ion conductivity tests were performed on these membranes, and the MgO-LHIC composite membrane (15.1 mS cm^{-1}) exhibited slightly lower conductivity than the porous polyolefin membrane (16.7 mS cm^{-1}) (Fig. 3f and S18†).

To qualitatively analyze the ionic selectivity of the MgO-LHIC composite membrane (Fig. 3g), drift-diffusion tests on MgO-LHIC and porous polyolefin membranes were conducted using a KCl solution with a concentration gradient of 10 (*trans*/*cis* = 100 mM/10 mM).[40,41] The essential parameters such as the short-circuit current (I_{SC}) and reversal potential (E_{rev}) were measured to evaluate the charged state of membranes for ion selectivity. Under the concentration gradient of *trans*/*cis* = 100 mM/10 mM, a negative I_{SC} and a positive E_{rev} indicate the anodic selectivity for the blank polyolefin membrane. In contrast, a positive I_{SC} and a negative E_{rev} of the MgO-LHIC composite membrane revealed its cationic selectivity feature. To further investigate the electrostatic repulsion of the membrane, zeta potentials were comparatively measured on the MgO-LHIC composite membrane and porous polyolefin membrane (Fig. 3h). The MgO-LHIC composite membrane presented a negative zeta potential of −1.71 mV originating from the adsorbed negatively charged iodine species in MgO-LHIC, while the porous polyolefin membrane exhibited a positively charged potential of 5.56 mV. The magnitude of zeta potential indicates the degree of electrostatic repulsion, with a negative zeta potential representing a net negative charge on the membrane surface. Therefore, compared with a blank porous polyolefin membrane, the MgO-LHIC composite membrane could accommodate the electrostatic repulsion properties against the permeation of active anions, *i.e.*, the polyiodides I_3^- and I_5^-, based on the Donnan repulsion effect. Taken together, these results demonstrate the strong chemical adsorption between MgO and iodine based on the adduct formation, where a concentrated negative charge layer onto the membrane facing the cathode side could effectively suppress the shuttling of polyiodide anions (Fig. 3i).

Electrochemical performance of ZIFBs at different temperatures

The electrochemical performance of ZIFBs was tested to evaluate the effect of the MgO-LHIC composite membrane. The MgO-LHIC composite membrane was pretreated in the iodine catholyte of simulated 50% SOC (Fig. S19†) and the configuration details of the flow cells are shown in Fig. S20 and S21.† Specifically, the CE increased from 98.2% to 99.5% as the current density varied from 10 mA cm^{-2} to 100 mA cm^{-2} in MgO-LHIC assembled ZIFBs (Fig. 4a and S22†). The corresponding voltage profiles of ZIFBs using the MgO-LHIC composite membrane are revealed in Fig. 4b. Even at a high current density of 50 mA cm^{-2}, the EE reached 58.3%, significantly higher than that of the porous polyolefin membrane (55.1%) (Fig. S23 and S24†), due to the lower permeability of the MgO-LHIC composite membrane to polyiodides.

Based on the discharge polarization and power density curves in Fig. 4c, the highest power density of batteries assembled with a MgO-LHIC composite membrane was 73.1 mW cm^{-2} at a current density of 110 mA cm^{-2}. In contrast, blank porous polyolefin membrane-based ZIFBs only achieved a peak power density of 63.4 mW cm^{-2} at a current density of 100 mA cm^{-2}. At a high volumetric capacity of 17.8 Ah L^{-1} (50% SOC, 20 mA h cm^{-2}), the ZIFBs based on the MgO-LHIC membrane delivered almost no capacity decay observed after 170 cycles (Fig. 4d and e), whereas the unmodified blank membrane exhibited significant deterioration within 60 cycles (Fig. 4f and g). Moreover, the CE and EE of MgO-LHIC composite membrane-based ZIFBs reached 96.3% and 68.6% in 170 cycles, respectively, far surpassing the CE (78.2%) and EE (61.9%) of blank porous polyolefin membrane-based ZIFBs in 60 cycles. This further validates the effectiveness of suppression on iodine crossover by the LHIC-based membrane. Meanwhile, ultraviolet-visible spectroscopy (UV-vis) was used to evaluate the cycled anolyte to further examine the selectivity of the membrane. As shown in Fig. S25,† there was no significant change in anolyte absorbance of the MgO-LHIC composite

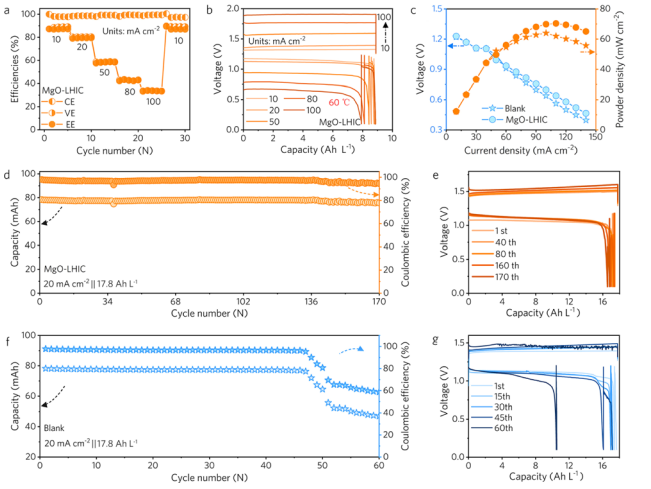

Fig. 4 (a) CE, VE, and EE of ZIFBs based on the MgO-LHIC composite membrane at different current densities. (b) Charge–discharge curves of the MgO-LHIC composite membrane-based ZIFBs at different current densities. (c) The voltage and power density of the ZIFBs based on the porous polyolefin membrane and MgO-LHIC composite membrane, respectively. (d and e) The cycling performance of ZIFBs at 20 mA cm^{-2} based on the MgO-LHIC composite membrane and the corresponding capacity–voltage profiles at different cycles. (f and g) The cycling performance of ZIFBs at 20 mA cm^{-2} based on the porous polyolefin membrane and the selected capacity–voltage profiles.

membrane-based ZIFBs before and after 50 cycles, which could be ascribed to the effective inhibition of iodine crossover. It should be noted that the iodine shuttle effect could not be completely avoided (as inferred from the low current CE). The shuttled iodine might spontaneously react with zinc, forming the zinc iodide solution, which could lead to the absence of detectable iodine in the anolyte. This further demonstrated the reversibility of ZIFBs. Furthermore, the surface morphology of the MgO coating showed no significant change after cycling in Fig. S26,† compared to that before cycling. And the zeta potential of the MgO composite membrane remained negative after 50 cycles (−2.04 mV), as shown in Fig. S27,† showing a slight increase from the initial value (−1.71 mV), as displayed in Fig. 3g, due to the adsorption of additional I_x^- during cycling. These results showed good stability of the MgO coating. Additionally, the testing was also applied for N117 membranes and carbon layer composite membranes under the same conditions. Although the CE of N117-based ZIFBs remained above 98% during the initial 15 cycles, the rapid failure of the battery was observed in subsequent cycles due to zinc dendrite penetration through the separator (Fig. S28 and S29†). As shown in Fig. S30,† the initial coulombic efficiency (93%) of the carbon layer membrane-based batteries at 10 mA cm^{-2} was lower than that of the MgO-LHIC membrane-based flow batteries (>98%) (Fig. 4a), suggesting that the MgO-LHIC layer is more effective for the suppression of polyiodide shuttling. The above results indicate that, compared with the blank porous polyolefin and N117 membranes, the as-developed MgO-LHIC composite membrane could not only lead to higher energy efficiency but also to superior cycling stability of ZIFBs.

To evaluate the energy storage application of a flow battery in high-temperature regions, the ZIFBs based on MgO-LHIC composite membranes were characterized at a high temperature (60 °C), as shown in Fig. 5a and S31.† First, the rate performance of MgO-LHIC-assembled ZIFBs exhibited an increment in CE from 94% to 98% as the current density range varied from 10 mA cm^{-2} to 100 mA cm^{-2} (Fig. 5b and S32†), significantly better than those of blank porous polyolefin membrane-assembled ZIFBs (Fig. S33†). MgO-LHIC composite membranes exhibited superior suppression of active iodine cross-over, particularly at high temperatures. Moreover, the corresponding voltage profiles of ZIFBs using different membranes are presented in Fig. 5c and S34.† The discharge polarization and power density curves of blank porous polyolefin and MgO-LHIC composite membranes are presented in Fig. 5d. They reveal that the batteries assembled with MgO-LHIC composite membranes could achieve a maximum power density of 70.4 mW cm^{-2} at a current density of 110 mA cm^{-2}. Comparatively, the ZIFBs assembled with porous polyolefin membranes only reached a peak power density of 55.7 mW cm^{-2} at a current density of 80 mA cm^{-2}. At a high volumetric capacity of 17.8 Ah L^{-1} (50% SOC, 20 mA h cm^{-2}), ZIFBs assembled with LHIC membranes exhibited minimal capacity decay over 75 cycles at a high temperature of 60 °C, while unmodified membranes displayed obvious degradation within only 11 cycles (Fig. 5e–g). Furthermore, the CE and EE of MgO-LHIC composite membrane-based ZIFBs reached 95.1% and 67.5% in 75 cycles, respectively, far surpassing the CE (61.1%) and EE (46.8%) of porous polyolefin membranes before 12 cycles. Even at a high temperature of 60 °C, the improved performance of ZIFBs assembled with MgO-LHIC composite membranes can be attributed to the stable adduct of MgO–iodine, which can effectively suppress the shuttling effect based on the Donnan exclusion as well as the concentration gradient effect.

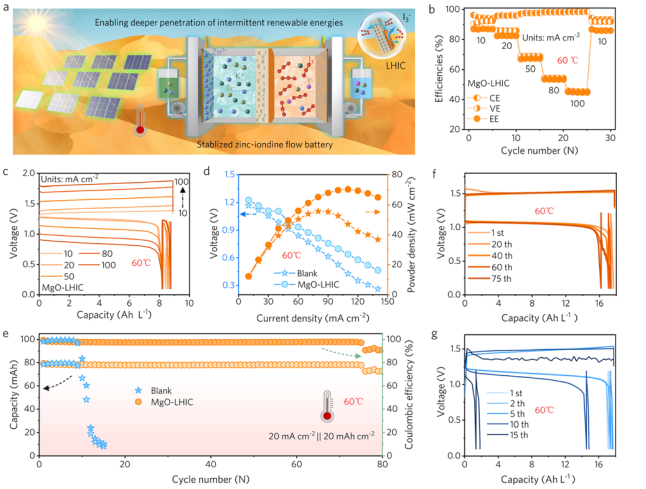

Fig. 5 (a) Schematic of ZIFBs for energy storage applications in high temperature regions. (b) CE, VE, and EE of ZIFBs based on blank porous polyolefin and MgO-LHIC composite membranes. (c) The charge–discharge curves of the MgO-LHIC composite membrane-based ZIFBs at different current densities. (d) The voltage and power density diagram of ZIFBs at different current densities based on porous polyolefin and MgO-LHIC composite membranes. (e) The cycling performance of ZIFBs at 20 mA cm^{-2} based on blank porous polyolefin and MgO-LHIC composite membranes and (f and g) the corresponding capacity–voltage profiles at different cycles, respectively.

Conclusions

In summary, LHIC-based composite membranes were pioneeringly developed by introducing a LHIC-based coating layer onto cost-effective porous polyolefin membranes, where the LHIC was constructed by exploiting the adduct chemistry to form strong chemical adsorption between the iodine species and a series of low-cost oxides (*e.g.*, MgO, CeO_2, ZrO_2, TiO_2, and Al_2O_3). Having the strongest and most stable iodine adsorption capability, the MgO-LHIC composite membrane can suppress the iodine crossover most effectively by Donnan repulsion and concentration gradient effects. At a high volumetric capacity of 17.8 Ah L^{-1}, the CE/EE of the LHIC composite membrane remained above 96.3%/68.6% in 170 cycles, far exceeding the values (78.2%/61.9%) of the porous polyolefin membrane in 60 cycles. Even at a high temperature of 60 °C, the ZIFB based on the MgO-LHIC composite membrane effectively suppressed iodine shuttling and enabled a significantly higher CE than that of the porous polyolefin membrane. It should be noted that various low-cost oxides (*i.e.*, MgO, CeO_2, ZrO_2, TiO_2, and Al_2O_3) are verified applicable for the LHIC-based membrane, where it

embodies the effectiveness of applying the Donnan repulsion force by building a LHIC layer to inhibit the shuttling of the active polyiodides in ZIFBs. This work presents a cost-effective and easily applicable strategy to exploit low-cost membranes for zinc–iodine flow batteries to address the cross-over issue by polyiodide species, paving the way for the practical application of ZIFBs.

Data availability

The data supporting this article have been included as part of the ESI.†

Author contributions

Y. C. Hu and T. Hu: formal analysis, data curation, investigation, validation. Y. W. Zhang, H. C. Huang, Y. X. Pei, Y. H. Yang, and Y. D. Wu: formal analysis, validation, visualization. H. M. Cheng: writing – review & editing. H. B. Hu and G. J. Liang: formal analysis, funding acquisition, project administration, supervision, writing – original draft, writing – review & editing.

Conflicts of interest

There are no conflicts to declare.

Acknowledgements

This work was financed by the Shenzhen Science and Technology Program (JCYJ20230807142508016), Guangdong Basic and Applied Basic Research Foundation (2024A1515010915), Excellent Youth Fund of Anhui Province (2108085Y17), Innovation and Entrepreneurship Support Plan of Anhui Province for Returned Personnels Studying Abroad (2022LCX001), Hundred-Talent Program of Anhui Province, and State Key Laboratory of New Textile Materials and Advanced Processing Technologies (No. FZ20230010).

References

1 M. Park, J. Ryu, W. Wang and J. Cho, *Nat. Rev. Mater.*, 2016, **2**, 16080.
2 R. Feng, X. Zhang, V. Murugesan, A. Hollas, Y. Chen, Y. Shao, E. Walter, N. P. N. Wellala, L. Yan, K. M. Rosso and W. Wang, *Science*, 2021, **372**, 836.
3 G. L. Soloveichik, *Chem. Rev.*, 2015, **115**, 11533.
4 (*a*) G. Liang, B. Liang, A. Chen, J. Zhu, Q. Li, Z. Huang, X. Li, Y. Wang, X. Wang, B. Xiong, X. Jin, S. Bai, J. Fan and C. Zhi, *Nat. Commun.*, 2023, **14**, 1856; (*b*) Y. Yang, G. Qu, H. Wei, Z. Wei, C. Liu, Y. Lin, X. Li, C. Han, C. Zhi and H. Li, *Adv. Energy Mater.*, 2023, **13**, 2203729.
5 G. Liang, F. Mo, X. Ji and C. Zhi, *Nat. Rev. Mater.*, 2021, **6**, 109.
6 P. Zuo, Y. Li, A. Wang, R. Tan, Y. Liu, X. Liang, F. Sheng, G. Tang, L. Ge, L. Wu, Q. Song, N. B. McKeown, Z. Yang and T. Xu, *Angew. Chem., Int. Ed.*, 2020, **59**, 9564.
7 F. Ai, Z. Wang, N. C. Lai, Q. Zou, Z. Liang and Y. C. Lu, *Nat. Energy*, 2022, **7**, 417.
8 R. Feng, X. Zhang, V. Murugesan, A. Hollas, Y. Chen, Y. Shao, E. Walter, N. P. N. Wellala, L. Yan, K. M. Rosso and W. Wang, *Science*, 2021, **372**, 836.
9 (*a*) B. Liu, C. W. Tang, W. Wei, C. Zhang, G. Jia and T. Zhao, *Energy Storage Mater.*, 2023, **60**, 102808; (*b*) Z. Q. Wei, Z. D. Huang, G. J. Liang, Y. Q. Wang, S. X. Wang, Y. H. Yang, T. Hu and C. Y. Zhi, *Nat. Commun.*, 2024, **15**, 3841.
10 Z. Yuan, Y. Yin, C. Xie, H. Zhang, Y. Yao and X. Li, *Adv. Mater.*, 2019, **31**, 1902025.
11 J. Zhang, G. Jiang, P. Xu, A. Ghorbani Kashkooli, M. Mousavi, A. Yu and Z. Chen, *Energy Environ. Sci.*, 2018, **11**, 2010.
12 D. Lin and Y. Li, *Adv. Mater.*, 2022, **34**, 2108856.
13 M. Mousavi, H. Dou, H. Fathiannasab, C. J. Silva, A. Yu and Z. Chen, *Chem. Eng. J.*, 2021, **412**, 128499.
14 C. Xie, Y. Liu, W. Lu, H. Zhang and X. Li, *Energy Environ. Sci.*, 2019, **12**, 1834.
15 Q. P. Jian, M. C. Wu, H. R. Jiang, Y. K. Lin and T. S. Zhao, *J. Power Sources*, 2021, **484**, 229238.
16 G. M. Weng, Z. Li, G. Cong, Y. Zhou and Y. C. Lu, *Energy Environ. Sci.*, 2017, **10**, 735.
17 (*a*) S. Ito, M. Sugimasa, Y. Toshimitsu, A. Orita, M. Kitagawa and M. Sakai, *Electrochim. Acta*, 2019, **319**, 164; (*b*) Z. Li, W. Cao, T. Hu, Y. Hu, R. Zhang, H. Cui, F. Mo, C. Liu, C. Zhi and G. Liang, *Angew. Chem., Int. Ed.*, 2024, **63**, e202317652.
18 L. Gao, Y. Ding, G. He and G. Yu, *Small*, 2022, **18**, 2107055.
19 (*a*) F. Wang, J. Tseng, Z. Liu, P. Zhang, G. Wang, G. Chen, W. Wu, M. Yu, Y. Wu and X. Feng, *Adv. Mater.*, 2020, **32**, 202000287; (*b*) T. Hu, Y. Zhao, Y. Yang, H. Lv, R. Zhong, F. Ding, F. Mo, H. Hu, C. Zhi and G. Liang, *Adv. Mater.*, 2024, **36**, 2312246.
20 R. Tan, A. Wang, R. Malpass-Evans, R. Williams, E. W. Zhao, T. Liu, C. Ye, X. Zhou, B. P. Darwich, Z. Fan, L. Turcani, E. Jackson, L. Chen, S. Y. Chong, T. Li, K. E. Jelfs, A. I. Cooper, N. P. Brandon, C. P. Grey, N. B. McKeown and Q. Song, *Nat. Mater.*, 2020, **19**, 195.
21 C. Ye, A. Wang, C. Breakwell, R. Tan, C. Grazia Bezzu, E. Hunter-Sellars, D. R. Williams, N. P. Brandon, P. A. A. Klusener, A. R. Kucernak, K. E. Jelfs, N. B. McKeown and Q. Song, *Nat. Commun.*, 2022, **13**, 3184.
22 Y. Ding and G. Yu, *Angew. Chem., Int. Ed.*, 2016, **55**, 4772.
23 B. Hu, J. Luo, M. Hu, B. Yuan and T. L. Liu, *Angew. Chem., Int. Ed.*, 2019, **58**, 16629.
24 D. Ma, B. Hu, W. Wu, X. Liu, J. Zai, C. Shu, T. Tadesse Tsega, L. Chen, X. Qian and T. L. Liu, *Nat. Commun.*, 2019, **10**, 3367.
25 B. Li, Z. Nie, M. Vijayakumar, G. Li, J. Liu, V. Sprenkle and W. Wang, *Nat. Commun.*, 2015, **6**, 6303.
26 A. Hollas, X. Wei, V. Murugesan, Z. Nie, B. Li, D. Reed, J. Liu, V. Sprenkle and W. Wang, *Nat. Energy*, 2018, **3**, 508.
27 X. Lou, D. Yuan, Y. Yu, Y. Lei, M. Ding, Q. Sun and C. Jia, *Chem.–Asian J.*, 2020, **15**, 2357.
28 N. Chang, Y. Yin, M. Yue, Z. Yuan, H. Zhang, Q. Lai and X. Li, *Adv. Funct. Mater.*, 2019, **29**, 1901674.

29 Z. Yuan, X. Liu, W. Xu, Y. Duan, H. Zhang and X. Li, *Nat. Commun.*, 2018, **9**, 3731.
30 X. X. Hou, K. Huang, Y. S. Xia, F. Y. Mu, H. Y. Cao, Y. Xia, Y. L. Wu, Y. Q. Lu, Y. X. Wang, F. Xu, Y. Yu, W. H. Xing and Z. Xu, *AIChE J.*, 2022, **68**, e17738.
31 C. Xie, H. Zhang, W. Xu, W. Wang and X. Li, *Angew. Chem., Int. Ed.*, 2018, **13**, 11341.
32 Z. Yuan, X. Zhu, M. Li, W. Lu, X. Li and H. Zhang, *Angew. Chem., Int. Ed.*, 2016, **55**, 3058.
33 S. Peng, L. Zhang, C. Zhang, Y. Ding, X. Guo, G. He and G. Yu, *Adv. Energy Mater.*, 2018, **8**, 1802533.
34 Q. Dai, Z. Liu, L. Huang, C. Wang, Y. Zhao, Q. Fu, A. Zheng, H. Zhang and X. Li, *Nat. Commun.*, 2020, **11**, 13.
35 H. Dou, M. Xu, B. Wang, Z. Zhang, D. Luo, B. Shi, G. Wen, M. Mousavi, A. Yu, Z. Bai, Z. Jiang and Z. Chen, *Angew. Chem., Int. Ed.*, 2021, **60**, 5864.
36 L. Zhang, Y. Ding, C. Zhang, Y. Zhou, X. Zhou, Z. Liu and G. Yu, *Chem*, 2018, **4**, 1035.
37 Z. Li and Y. C. Lu, *Nat. Energy*, 2021, **6**, 517.
38 J. Häggström, D. Balyozova, K. J. Klabunde and G. Marchin, *Nanoscale*, 2010, **2**, 529.
39 P. K. Stoimenov, V. Zaikovski and K. J. Klabunde, *J. Am. Chem. Soc.*, 2003, **125**, 12907.
40 Y. Ling, D. X. Yan, P. F. Wang, M. Wang, Q. Wen, F. Liu and Y. G. Wang, *Chin. Phys. Lett.*, 2016, **33**, 096103.
41 J. Zhou, Z. Jiao, Q. Zhu, Y. Li, L. Ge, L. Wu, Z. Yang and T. Xu, *J. Membr. Sci.*, 2021, **627**, 119246.